Journal Pre-proof

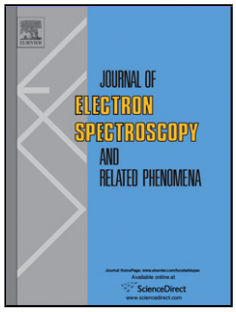

Assessment of structural order indices in Kaolinites: a multi-technique study including EXAFS

D. Richard, J.M. Martínez, M. Mizrahi, L. Andrini, N.M. Rendtorff

PII: S0368-2048(21)00079-7

DOI: https://doi.org/10.1016/j.elspec.2021.147128

Reference: ELSPEC 147128

To appear in: *Journal of Electron Spectroscopy and Related Phenomena*

Received Date: 18 June 2021

Revised Date: 15 September 2021

Accepted Date: 27 September 2021

Please cite this article as: Richard D, Martínez JM, Mizrahi M, Andrini L, Rendtorff NM, Assessment of structural order indices in Kaolinites: a multi-technique study including EXAFS, *Journal of Electron Spectroscopy and Related Phenomena* (2021), doi: https://doi.org/10.1016/j.elspec.2021.147128

Assessment of structural order indices in Kaolinites: a multi-technique study including EXAFS

D. Richard[1,2]*, J. M. Martínez[1,2], M. Mizrahi[2,3,4], L. Andrini[2,4] and N. M. Rendtorff[1,2]

[1]*CETMIC, Centro de Tecnología de Recursos Minerales y Cerámica (CONICET La Plata - CIC PBA - UNLP). Camino Centenario y 506, CC 49, (B1897ZCA), M. B. Gonnet, Buenos Aires, Argentina.*

[2]*Facultad de Ciencias Exactas, Universidad Nacional de La Plata. 47 y 115, La Plata, Buenos Aires, Argentina.*

[3]*Facultad de Ingeniería, Universidad Nacional de La Plata. 1 y 47, La Plata, Buenos Aires, Argentina.*

[4]*INIFTA, Instituto de Fisicoquímica Teórica y Aplicada (UNLP-CONICET La Plata). 64 y diagonal 113, 1900 La Plata, Argentina*

*E-mail: richard@fisica.unlp.edu.ar

Highlights

- Kaolinite structural order indices from each experimental technique are determined
- Different structure scales were covered: crystallographic, superficial, and local
- Experimental outputs were compared with signals based on a DFT theoretical structure
- EXAFS Debye-Waller factor is well suited for describing structural order

Abtract

This work presents a study of the structural properties on four representative kaolinite samples. Scanning Electron Microscopy (SEM), X-ray Diffraction (XRD), Thermochemical Analyses (DTA/TGA), and X-ray Near Edge Structure (XANES) and Extended X-ray Absorption Fine Structure (EXAFS) spectroscopy measurements were carried out, and different empirical indices that quantify the structural order were assessed. Also, XRD patterns and EXAFS signals were compared to those corresponding to idealized defect-free structures calculated theoretically, to analyze the effects related to the structural disorder on real samples. The structural order at different scales (crystallographic, superficial, and local) was comprehensively examined for the four samples, and correlations between the order indices were performed and discussed, including the Debye-Waller factor obtained from Si K-edge EXAFS measurements. The proposed methodology shows that

EXAFS is a suitable complementary technique that can provide valuable information about the Si local environments in natural kaolinites.

Keywords: kaolinite structure, EXAFS, XRD, DFT, order indices, DW factor.

1. Introduction

Kaolinite is a natural clay material widely spread in Earth's crust, which has been used for hundreds of years in a large variety of technological applications (Schroeder & Erickson, 2014; Dill, 2016). Nowadays, kaolinitic clays are used in the industry to produce ceramics, cement, refractories, pharmaceuticals, paper, plastics, etc. In many cases prior thermal treatments are needed to reach such industrial applications (Rashad, 2013; Tironi *et al.*, 2014).

The structure of kaolinite has been studied during almost eighty years, starting with the work of Brindley and Robinson (1945). Since then, different approaches have emerged in order to get a deeper understanding of it. In the last years, experimental, theoretical and combined strategies have been proposed to analyze different aspects of the kaolinite structure and its modifications induced by heating (White *et al.*, 2010; Tunega *et al*, 2012; White *et al.*, 2013; Paris, 2014; Weck *et al.*, 2015; Andrini *et al.*, 2016; Drits *et al.*, 2019; Kloprogge, 2019; Richard & Rendtorff, 2019). Knowledge of the structural variations is used to understand natural systems (Balan *et al*., 2007), and also needed for industrial applications, because of their correlation with plasticity, brightness and viscosity (Aparicio & Galán, 1999).

From the experimental point of view, different approaches and models have been proposed to gain insights about the differences between kaolinite samples. Among them, X-ray diffraction (XRD) is a very useful technique for a crystallographic characterization, because kaolinites occur as fine particles (Sakharov *et al.*, 2016, Leonardi & Bish, 2020). The mathematical modeling of XRD patterns can improve the description of various structural defects and polytypes in kaolinites (Plançon *et al.*, 1988; Sakharov *et al.*, 2016). Nevertheless, the complex disordered nature of the samples makes such refinement tools difficult to implement in routine studies of kaolins. Then, global crystallinity indices

calculated from XRD patterns are very common in the literature, because they are based in simple and expeditious procedures that allow a quantification of the sample 'crystallinity' (Guggenheim *et al.*, 2002). During the last decades, many empirical indices based on XRD peak intensity ratios have emerged to quantitatively measure the state of order-disorder in kaolinites (Aparicio & Galán, 1999; Aparicio *et al.*, 2006). On the other hand, clay processing usually leads to structure amorphization, then, to reach a comprehensive understanding of the sample structure, XRD should be complemented by other experimental techniques that are not affected by the loss of crystallinity and allow the measurement of structural ordering at short distances. In this way, techniques that focus on the local atomic environments emerge as good alternatives to follow the structural transformations during clay processing. Among them are found X-ray Absorption Spectroscopies (XAS) such as X-ray Absorption Near Edge Structure (XANES) and Extended X-ray Absorption Fine Structure (EXAFS) spectroscopies, and also other techniques such as infrared and Raman spectroscopies, Nuclear Magnetic Resonance (NMR), Electron Paramagnetic Resonance (EPR), and Mössbauer spectroscopy (Barreto Maia *et al.*, 2014; Paris, 2014; Andrini *et al.*, 2016; Danner *et al.*, 2018; Kloprogge, 2019). Currently, the relation between crystallographic, the nano- and micro- structural order and the clay performance for different technological applications is still a matter of study (Johnston, 2010; Gadikota *et al.*, 2017; Li *et al.*, 2019).

XAS techniques are among the best options to characterize the electronic and structural properties of materials. One of the main advantages of XAS techniques is that they are chemically selective, enabling the study of each atomic element present in the sample to be analyzed individually, being able to obtain information of the oxidation state of the atoms, average coordination number, interatomic distances and degree of disorder from the atomic environment to the absorbing atom (Bunker, 2010). Unlike XRD, XAS spectroscopies do not need a system with long-range order, so non-crystalline phases present in the samples could be studied. Furthermore, performing XAS measurements in the transmission geometry, the information obtained is representative of the whole volume of the particles and not just of the surface. For all these reasons, XAS is one of the most versatile techniques for the electronic and structural characterization of this kind of systems (Rivard *et al*., 2013; Dumas *et al.*, 2015; Pietzsch et al., 2015; Andrini et al., 2019).

This work presents a comparison of the structural order using direct and indirect parameters on four representative kaolinite samples. For a standard characterization of raw materials, Scanning Electron Microscopy (SEM), XRD and thermochemical analyses, which include Differential Thermal Analysis (DTA) and Thermal Gravimetric Analysis (TGA), were used. In addition, EXAFS at the Si K-edge measurements were performed and analyzed.

The aim of this study is to assess the sensitivity of each experimental technique to quantify the structural order-disorder on kaolinites through the determination of different empirical indices. The final motivation is to find the best experimental techniques adapted for the study of natural samples, which are more complex than reference standards and idealized structures, and are actually the ones commonly used in industry. To this purpose, standard and commercial kaolinites were considered in this study. Firstly, XRD and DTA typical prompt empirical indices were determined for the different samples. Then, the XRD patterns and also the EXAFS signals were compared to those corresponding to a defect-free and totally crystalline kaolinite structure, which was theoretically determined by first-principles calculations based on Density Functional Theory (DFT). This procedure is quite straightforward using current available computational codes, and allows accessing to hypothetical experimental results if a totally crystalline kaolinite were measured. Therefore, the combination of experiments with theoretical predictions allows a deeper understanding of the samples, because from the observed differences between experiments and predictions it can be inferred how the degree of structural disorder in real samples affects the results provided by the techniques. Finally, correlations between the order indices were analyzed, including the Debye-Waller factor obtained from EXAFS measurements. This procedure provides links between the different structural scales these indices cover (crystallographic, superficial, and local), and also serves to assess each index performance to distinguish among samples according to the kind of structural order it measures.

2. Materials and methods

2.1. Kaolinite structure and raw materials

Structurally, kaolinite is a hydrous aluminum silicate with the ideal formula $Al_2Si_2O_5(OH)_4$, classified as a 1:1 dioctahedral phyllosilicate. It consists of alumina octahedral sheets and silica tetrahedral sheets alternately arranged in an almost perfect 1:1 layer structure (Brigatti *et al.*, 2006). According to the experimental data, kaolinite belongs to the triclinic system and the space group of symmetry is C1 (Bish, 1993; Neder *et al.*, 1999). The theoretical arrangement of atoms and the unit cell in the kaolinite phase is shown in Fig. 1. The Si atoms are tetrahedrally coordinated by oxygen atoms, and the Al atoms are octahedrally coordinated by oxygen atoms and hydroxyl groups, giving a theoretical composition of 46.54 wt. % SiO_2, 39.50 wt. % Al_2O_3 and 13.96 wt. % H_2O. Nevertheless, the crystal structure of real kaolinite samples is highly complex due to a variety of structural defects and stacking faults that may appear during its formation (Brigatti *et al.*, 2006; Sakharov *et al.*, 2016).

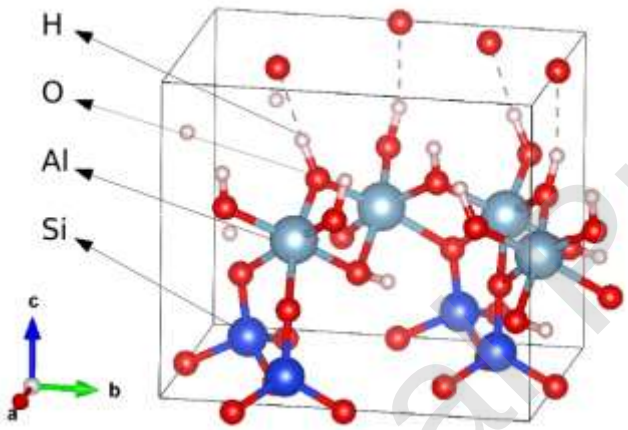

Figure 1. Structure of kaolinite and unit cell.

In this work, four kaolinite samples were considered: the reference standard samples KGa-1 and KGa-2 from the Source Clays Repository of The Clay Mineral Society (Mermut & Cano, 2001; Sakharov *et al.*, 2016), a commercial sample of Fisher Scientific, and a local washed kaolinitic clay C80 of Piedra Grande S.A. The KGa-1 standard (Washington County, GA, USA) is often referred as a well crystallized kaolinite, while the KGa-2 sample (Warren County, GA, USA) has a more disordered structure (Sakharov *et al.*, 2016). Previous studies have reported a high kaolinite content (> 95%) for KGa-1 and KGa-2 samples (Chipera & Bish, 2001; Heide & Földvari, 2006). According to previous investigations the sample from Fisher (Georgia, USA) is also an almost pure kaolinite (~ 98%)

(Andrini *et al.*, 2016). On the other hand, the mineralogical composition of the C80 sample (Chubut, Argentina) consists of kaolinite (> 40%), and the rest is quartz and feldspar (Moreno Erazo 2014; Andrini *et al.*, 2016). This sample selection allows studying the different order indices in hard and soft reference kaolinites (KGa-1 and KGa-2, respectively), as well as a commercial kaolinite and a kaolinitic clay used in local industry (Fisher and C80, respectively).

2.2. General description of the methodology

2.2.1. Microstructural characterization. Considering that it is known that typical kaolinites are comprised of grains with sizes in the range 0.1-10 µm (Uwins *et al.*, 1993; Sei *et al.*, 2006; Johnston, 2010), a first approach to the structures of the four samples was done by performing a microstructural characterization by SEM (Fei Quanta 200). To this purpose, gold coated kaolinite powders over carbon tape were analyzed in ultra-high vacuum and 20 kV conditions, using an Everhart-Thornley detector in backscattered electron mode.

2.2.2. Powder XRD analysis. The kaolinite samples were also characterized by XRD (Philips 3020, Cu-Kα radiation, Ni filter, 40 kV-20 mA) in the 5°-70° *2θ* range. The order degree was analyzed from diffraction patterns by considering two well-established kaolinite 'crystallinity' indices: the Hinckley Index (HI) (Hinckley, 1963; Plançon *et al.*, 1988), and the R2 index after Lietard (Lietard, 1977; Aparicio *et al.*, 2006).

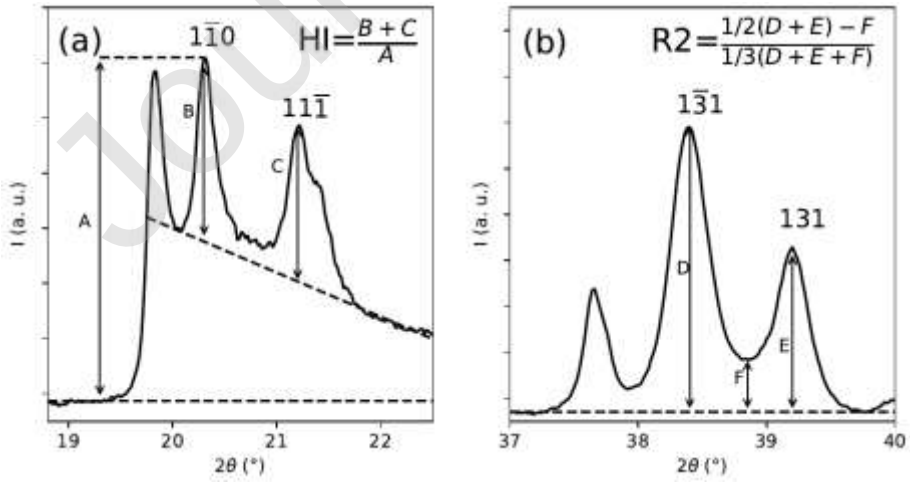

Figure 2. Method for the determination of order indices based on XRD: (a) HI and (b) R2.

HI is the ratio of the sum of the heights of the peaks $\overline{1}10$ and $\overline{1}11$ measured from the local background of the pattern, and the height of the $\overline{1}10$ peak measured from the general background (see Fig. 2a). This index allows a measurement of the kaolinite 'crystallinity' because it combines the resolution of these neighbor peaks, which depends on crystallinity due to random shifts between adjacent layers over *b*-axis, and the height of the $\overline{1}10$ peak, which depends on the frequency of defects. So, the algebraic procedure involved in the construction of the HI yields a dimensionless number that, depending on the considered sample, normally varies between 0.2 and 1.5, in a way that the larger the value of HI, the greater the 'crystallinity' (La Iglesia, 1993; Uwins *et al.*, 1993; Aparicio & Galán, 1999; Vieira-Coelho *et al.*, 2000; Valášková *et al.*, 2011; Tironi *et al.*, 2014; Sakharov *et al.*, 2016). In the hypothetical case of a perfect kaolinite structure, where the XRD pattern has no background, HI ~ 2. Alternatively, if the sample is treated as a mixture of a low- and high- defect phase, the HI is related to the relative proportions of these two kinds of kaolinites (Plançon *et al.*, 1988; Sakharov *et al.*, 2016).

On the other hand, the R2 index is sensitive to random defects only and involves the heights of the diffraction peaks $\overline{1}31$, and $\overline{1}31$, and the height of the inter-peak valley measured from the background (see Fig. 2b). In this case, larger values of R2 reflect a minor density of random defects into the kaolinite structure, in a way that R2 ~ 1.2 for a well-ordered kaolinite sample (Aparicio & Galán, 1999; Vieira-Coelho *et al*, 2000; Tironi *et al.*, 2014), and R2=1.5 for the XRD pattern of the perfect kaolinite structure.

2.2.3. DTA/TGA measurements. A characterization of the samples was performed by analyzing the effect of heat treatment on them. To this purpose, differential thermal (DTA) and thermogravimetric (TGA) analyses were simultaneously carried out on a Netzsch 409C equipment, with a 10 °C/min heating rate in Pt crucibles in air atmosphere. The TGA technique allows inferring the kaolinite purity, considering that dehydroxylation of pure kaolinite (produced between 500 and 600 °C) results in a theoretical mass loss of 13.9 wt. % of the initial amount (Steudel *et al.*, 2013). On the other hand, the DTA technique is based on energy changes, so it is especially suited to follow structural transformations during kaolinite heating. Many DTA studies have related the kaolinite crystallinity

with the position of the characteristic endothermic peak corresponding to the kaolinite-metakaolinite transition, showing that for poorly crystallized type of kaolins this endothermic reaction moves to lower temperatures (Chakraborty, 2014). Furthermore, in addition to the peak position, kaolinite surface defects can be quantified from the shape of this endothermic peak (Fig. 3a). In this sense, the Slope Ratio (SR) index is commonly used to characterize the amount of surface defects (Lietard, 1977; Bich *et al.*, 2009). SR index is defined as the ratio between the slope of the right branch and the slope of the left branch of the peak, after subtracting a background straight line for that region of temperatures (see Fig. 3b). For the ideal kaolinite, with a defect free surface, a symmetric endothermic peak is expected, which means SR=1. Otherwise, if surface defects are present, SR > 1 (La Iglesia, 1993; Sei *et al.*, 2006; Tironi *et al.*, 2012, 2014).

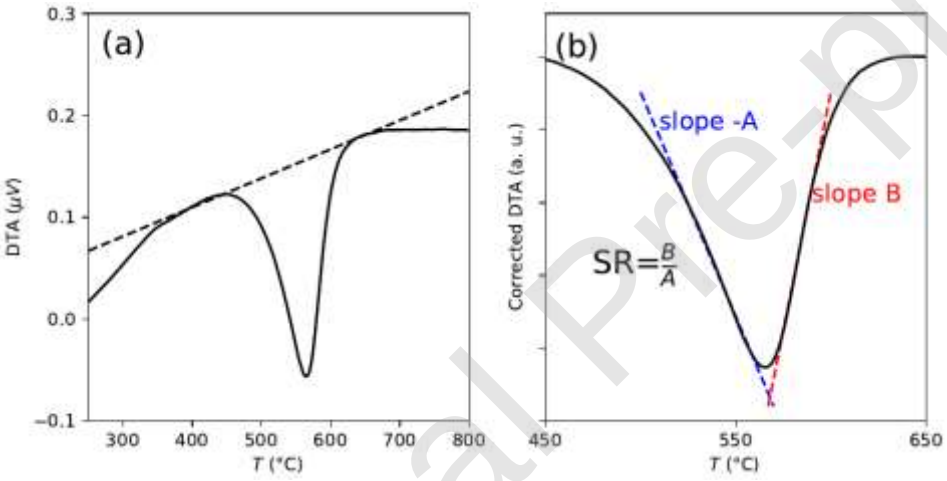

Figure 3. Method for the determination of the SR index based on DTA endothermic peak. (a) DTA curve and local background to be subtracted, and (b) corrected curve after background subtraction. The quantities A and B are defined positive.

2.2.4. XAS analysis. XAS experiments were performed at the SXS beamline from the Laboratorio Nacional de Luz Sincrotron (LNLS), Campinas, Brazil. Measurements at the Si (1839 eV) K-edge were carried out using a double-crystal monochromator equipped with InSb (111) crystals. The vertical slit opening was 1 mm for Si K-edge. Experiments were performed at room temperature in a vacuum of 10^{-9} mbar. The incident beam intensity (I_0) was measured using a thin foil of Au located before the main chamber. Kaolinite powder samples were attached on carbon tape to be measured in Total Electron Yield (TEY) mode, collecting the emitted current for each incident photon-energy with

an electrometer connected to the sample. The photon energies were calibrated using a Si^0 reference sample and setting the first inflection point to the theoretical energy of Si K-edge (at 1840 eV). The XANES spectra were normalized using standard procedures with the ATHENA software (Newville, 2001; Ravel & Newville, 2005). The baseline correction was made by subtracting a linear function from the pre-edge region at −30 to −10 eV relative to E_0 from the spectra, where E_0 is defined as the maximum in the first derivative, and the absorption coefficient $\mu(E)$ normalization was determined with a polynomial function across the post-edge region between 30 and 80 eV relative to E_0. EXAFS experiments at the Si K-edge were performed between 1800 and 2460 eV. The EXAFS oscillation was extracted from the spectra, and the Fourier Transform was calculated using the Hanning filtering function using the ATHENA software, and EXAFS modeling was carried out with ARTEMIS software, which are part of the IFFEFIT package (Ravel & Newville, 2005). The k^2 weighted $\chi(k)$ data, to enhance the oscillations at higher k, were Fourier transformed in the k range from 1.7 to 10.3 $Å^{-1}$. The bond lengths and Debye-Waller (DW) factor were obtained by a nonlinear least-squares fit of the theoretical EXAFS signal to the data in R-space by Fourier transformation of the experimental data in the range from 0.8 to 2.0 Å (without phase correction). Theoretical scattering path amplitudes and phase shifts for all paths used in the fits were calculated using the FEFF9 code (Rehr *et al.*, 2010). The passive reduction factor S_0^2 was fixed to the value of 0.86. This value was obtained fitting the EXAFS signal of SiO_2 reference, constraining the coordination number of the first coordination shell to 4. The effects of structural and vibrational disorder on the EXAFS signals are parameterized in terms of the DW factor. The amplitude and phase of the EXAFS signal are influenced by local disorder of thermal and static origin. EXAFS is generally more sensitive to disorder than XRD because of the higher values of momentum transfer. The effect of disorder on the amplitude of the EXAFS signal is generally accounted in the EXAFS equation for a factor $\exp(-2k^2\sigma^2)$, where σ^2 is the mean-square relative displacement (MSRD) of absorber and backscatterer atoms (Lee *et al.*, 1981). The peculiar sensitivity of the MSRD to the correlation of vibrational motion in crystals was recognized some decades ago (Beni & Platzman, 1976; Sevillano *et al.*, 1979), suggesting the use of EXAFS for checking the phase relationships between eigenvectors of the dynamical matrix obtained from *ab initio* or model calculations. In cases where coordination shells are not resolved, the distance found in the simulation for the combination of these unresolved shells

will be an average distance. The increased disorder in a shell, that is composed of nonresolved contributions (static disorder), is noted as a more rapid decline of the EXAFS amplitude at higher energy and a broadening of the peak in the Fourier transform; in the signal fit, this is reflected in a larger value for the DW factor.

2.3. Computational methods

The experimental results for the XRD patterns and the EXAFS signals were compared to a kaolinite structure determined from first-principles theoretical calculations in the work of Richard & Rendtorff (2019). This DFT structure is independent of any experiment and has the advantage of being exempted from the common limitations that an unique empirical technique may have. In particular, it was shown that it gathers those structural features that can be reached experimentally considering together the main strengths of neutron powder diffraction, single crystal XRD and nuclear magnetic resonance spectroscopy (Richard & Rendtorff, 2019). Then, in this work we extend the use of this DFT-based model to describe the structure at the crystallographic scale (through the simulation of the XRD pattern), and the kaolinite local properties at Si sites (by simulating the EXAFS signal). This procedure gives an additional framework to compare experiments and model. To simulate diffraction patterns from a known structure, the VESTA software was used (Momma & Izumi, 2011). On the other hand, EXAFS modeling was carried out using the FEFF9 code (Rher *et al.*, 2010).

3. Results

3.1. Microstructural characterization

Figure 4 shows representative SEM images of the studied clays. Typical clay agglomerates with clear platelet morphology were found in the four samples after scanning several random particles in each of them. In general, aggregates of hexagonal kaolinite plates can be described, but the edges show some breakage. Agglomerates size is about 5 μm, with predominant face to face and edge to edge contacts.

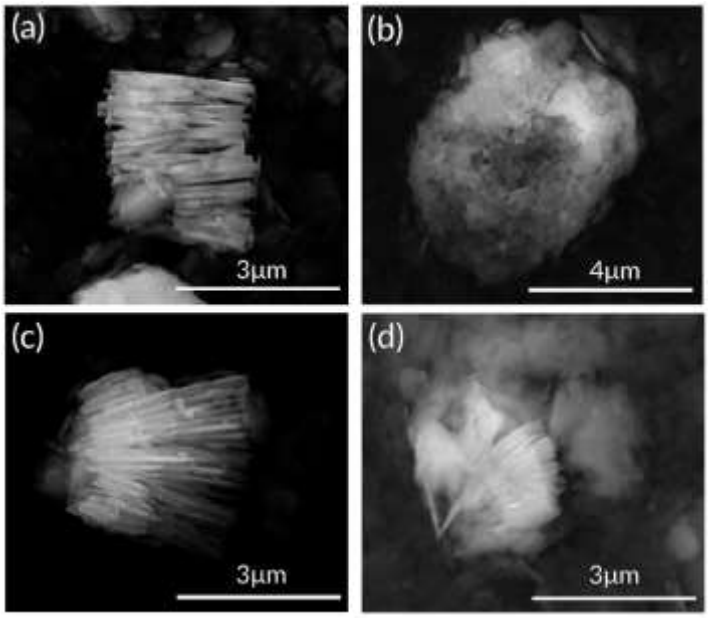

Figure 4. SEM images of the studied clays (a) KGa-1, (b) KGa-2, (c) Fisher, and (d) C80.

For KGa-1, C80 and Fisher particles, a sub-micronic sized internal structure of piled up layers can be identified. The KGa-1 micrograph (Fig. 4a) presents these layers with well-defined straight edges, as also observed for the Fisher sample (Fig. 4c). For KGa-1, those layers are arranged in a near straight stacking, while Fisher and C80 samples present a sided stacking, also known as the accordion morphology. In these three cases, lamina side and thickness are about 2-3 µm and 100 nm, respectively. Particularly, lamina thickness follows the sequence KGa-1>Fisher>C80. On the other hand, the KGa-2 clay also presents the platelet morphology, but arranged in bigger agglomerates with a different microstructure. The lamina sizes are about ten times smaller than those observed for the other kaolinites, and the stacking is not observed. These facts reflect the disorder or poorly crystallized character of the KGa-2 compared to the other three samples (Valášková e t al., 2011; Barreto Maia *et al.*, 2014). From this analysis it can be said, at this microscopical scale, that the grade of kaolinite structural definition follows the general sequence KGa-1>Fischer>C80>KGa-2.

3.2. Powder XRD

The XRD patterns corresponding to the studied samples are presented in Fig. 5a. For comparison purposes the patterns cover 2θ angles in the range 18°-43° and are normalized in a way so that the 020 peak intensities at 2θ= 20° are equal to each other. Figure 5a also shows in gray the simulated XRD pattern corresponding to the defect-free kaolinite structure determined from first-principles

calculations (Richard & Rendtorff, 2019), as aid to analyze how the presence of secondary phases or structure defects in real samples affects the ideal kaolinite XRD pattern. It must be noted that *ab initio* approaches slightly underestimate the experimental unit cell volumes, so minor shifts to higher 2θ values may be observed in the position of the predicted peaks compared to the experimental ones. In addition, the most prominent XRD lines corresponding to quartz (Kroll & Milko, 2003), anatase (Weirich *et al.*, 2000), and feldspar (Organova *et al.*, 1999) are also indicated in the top of the figure, because they are usual additional phases in kaolinite samples (Schoeder & Erickson, 2014; Andrini *et al.*, 2016).

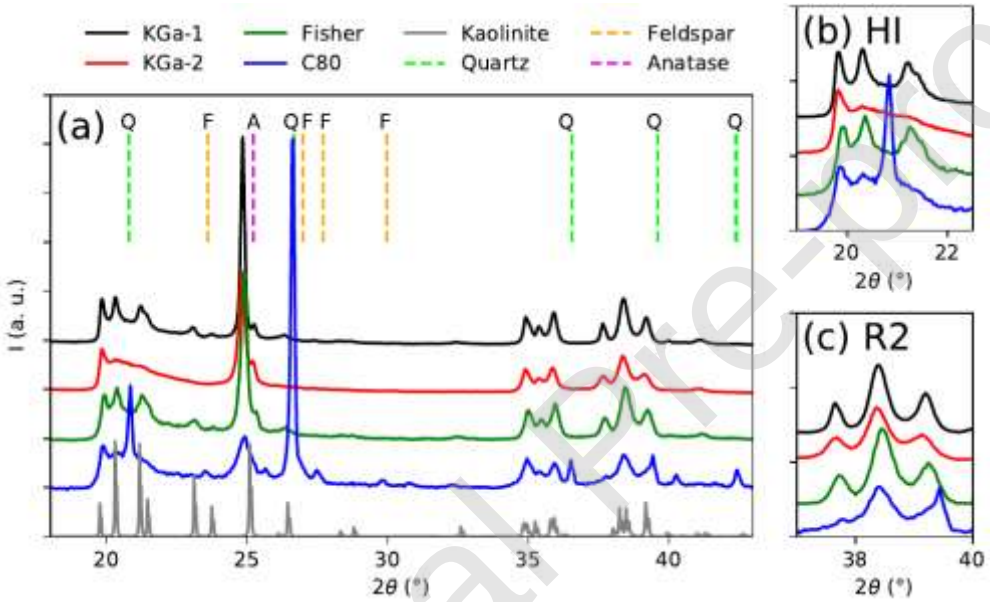

Figure 5. XRD patterns for the different samples. (a) Complete XRD patterns. The gray pattern in the bottom stands for the simulated pattern from the first-principles calculated structure of kaolinite (Richard & Rendtorff, 2019), while peaks of usual additional phases are indicated in the top. (b) Detail of the region corresponding to HI peaks and (c) R2 peaks.

From the comparison of measured and simulated XRD patterns, it can be seen that the samples present most of the peaks expected for the kaolinite structure, modified by the instrumental resolution (which increases the peak widths), and the presence of the XRD background related to the different structural disorders previously mentioned. In addition, a minor contribution of the anatase phase can be observed (see the shoulder in the peak at about 2θ= 25°). For the case of the C80 sample, prominent additional peaks corresponding to quartz are also present (at 2θ= 26.5° and 20.8°), which

are expected due to the substantial amount of quartz in this sample. Also, a minor contribution of the feldspar phase is present.

Figures 5b and 5c show a detail of the regions of the XRD pattern corresponding to HI and R2 indices (as sketched in Fig. 2). Samples KGa-1 and Fisher have better resolved peaks in the region 20-22°, in comparison to KGa-2 and C80 (see Fig. 5b). Nevertheless, a well defined value of HI can be determined in each case, with a relatively low error bar estimated from the graphical analises presented above (see error values in parentheses in Table 1). Both XRD-based indices, HI and R2 (Table 1), suggest an increasing crystallinity in the order KGa-2, C80, Fisher, and KGa-1. Nevertheless, this order should be taken with care when considering the values corresponding to the C80 sample, due to the significant presence of quartz (Aparicio & Galán, 1999). In this sense, in addition to the peak at 20.8° that can affect the determination of the HI value, quartz introduces a peak at about 39.5° that may interfere with the determination of the R2 index overestimating its value (see Fig. 5c).

	XRD		**DTA/TGA**			**EXAFS**	
Sample	**HI**	**R2**	T_{TGA} **(°C)**	T_{DTA} **(°C)**	**SR**	$R_{Si\text{-}O}$ **(Å)**	$DW_{Si\text{-}O}$ **(x10^{-3} Å^2)**
KGa-1	0.999(9)	0.97(1)	571	580	1.6(2)	1.62(1)	3.6(1)
KGa-2	0.30(2)	0.63(2)	556	571	2.2(5)	1.61(1)	9.4(2)
Fisher	0.86(2)	0.80(2)	598	612	1.2(4)	1.62(1)	5.8(2)
C80	0.45(4)	0.81(2)	547	565	2.0(3)	1.61* 1.62(1)	2.0* 8.6(2)

Table 1. Results for the different samples by XRD, DTA/TGA, and EXAFS: Hinckley Index (HI), R2 index after Lietard, kaolinite-metakaolinite transition temperatures from TGA (T_{TGA}) and DTA (T_{DTA}), Slope Ratio index (SR), Si-O interatomic distance ($R_{Si\text{-}O}$) and the Debye-Waller factor ($DW_{Si\text{-}O}$). For each value, the number in parentheses is the error in the last digit. *These parameters were kept fixed in the fit and correspond to the quartz phase.

3.3. DTA/TGA measurements

Thermogravimetric measurements in Fig. 6a show that for KGa-1, KGa-2, and Fisher samples most of the mass loss occurs between 500 and 600 °C, during the transition kaolinite-metakaolinite, and is about 14 wt. % of the initial amount, while for the C80 sample the loss at these temperatures is near 6 wt. % of the initial mass. Considering that theoretically the dehydroxylation of pure kaolinite results in a mass loss of 13.9 wt. % (Steudel *et al.*, 2013), for the clays KGa-1, KGa-2 and Fisher is inferred a kaolinite content near 100%, while for the C80 sample such amount is about 45%, in good agreement with the XRD measurements and other previous studies (Chipera & Bish, 2001; Heide & Földvari, 2006; Moreno Erazo, 2014; Andrini *et al.*, 2016).

On the other hand, the DTA curves (Fig. 7) show the characteristic peaks for kaolinites (Chakraborty, 2014). Between 500 and 650 °C the samples display the endothermic process corresponding to the kaolinite dehydroxylation, as shown also by the drastic mass loss from TGA curves. Near 1000 °C, DTA curves show an exothermic peak, due to the transformation of the metakaolinite into a spinel type aluminosilicate. In the case of the C80 sample, an additional endothermic peak is observed at about 100 °C, which is attributed to surface water loss, as is expected for a washed clay (Serra *et al.*, 2013; Conconi *et al.*, 2014; Bukalo *et al.*, 2018; Conconi *et al.* 2019). This effect was also reflected by the TGA curve of Fig. 6a for this clay.

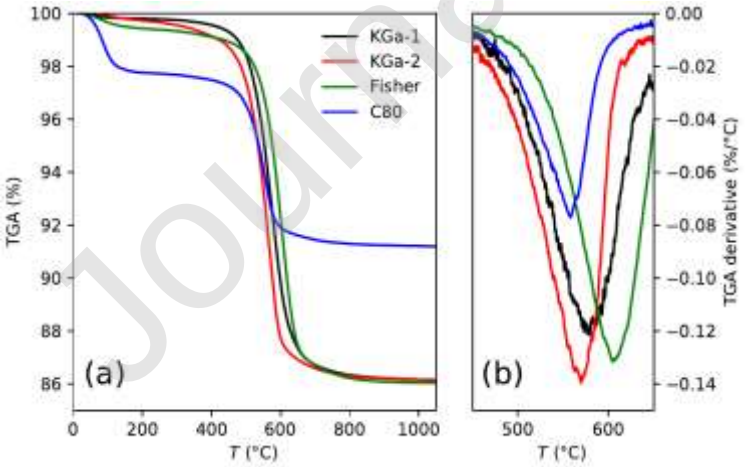

Figure 6. (a) TGA curves and (b) TGA derivatives (weight loss rate) in the kaolinite-metakaolinite transition region.

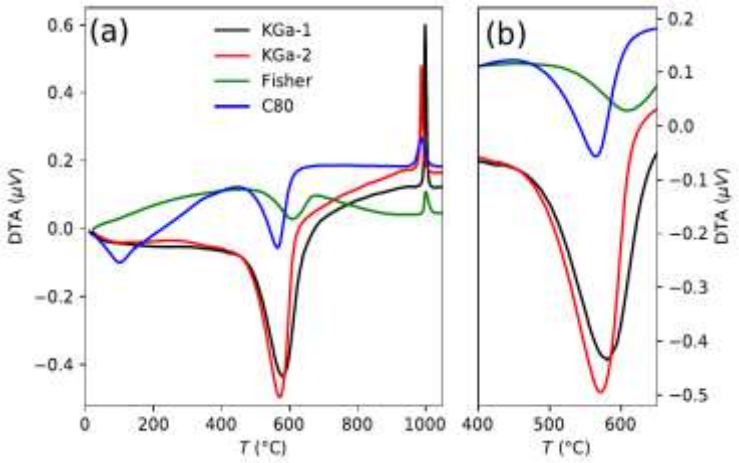

Figure 7. (a) DTA curves and (b) detail of the endothermic peaks corresponding to the kaolinite-metakaolinite transition.

A further study of the TGA and DTA curves reveals that the kaolinite-metakaolinite transition for these samples starts at different temperatures depending on the sample. The detail of TGA derivatives in the transition temperature region in Fig. 6b shows that, among the four samples, the C80 has the TGA derivative peak at the lowest temperature, and the Fisher one at the highest. In Table 1, the value of the TGA derivative peak temperature, T_{TGA}, obtained after fitting Gaussian curves to the derivative experimental data, is reported for each sample. The obtained results show that the temperature T_{TGA} increases in the order C80, KGa-2, KGa-1, and Fisher. This behavior is observed again when analyzing the endothermic peak position in the DTA signal (see Fig. 7b), as stated above. In Table 1, the corresponding peak temperatures during the dehydration process, T_{DTA}, are also summarized. On the other hand, the asymmetry of the DTA peaks of Fig. 7b were analyzed with the SR index. The corresponding values are given in Table 1. As can be seen, the SR results show that surface crystallinity increases in the order KGa-2, C80, KGa-1, and Fisher. Considering the error bars in SR, this order is in agreement with the order found for the T_{TGA} and T_{DTA} temperatures and suggests a correlation between such quantities.

3.4. EXAFS

Figure 8a shows the XAS spectra at the K edge of Si for the different samples, and Figure 8b the region near the absorption edge (Si K XANES). As can be seen, all the spectra have the same absorption edge energy (first inflection point of the curve), which corresponds to Si(IV), as expected

(Chaboy *et al.*, 2007). In addition, all the post-edge resonances present are similar to those reported by other authors for this type of clays (Ildefonse *et al*., 1995; Rivard *et al.*, 2013; Andrini *et al.*, 2016). In all cases an intense white line (≈ 1846 eV, feature A in Fig. 8b) is observed due to the allowed transition of Si 1*s* electrons to the antibonding 3*p*-like state (Li *et al.*, 1995) and related to tetrahedral coordination (White *et al.*, 2011). Furthermore, the spectrum corresponding to the KGa-2 sample shows a decrease of the order of 20 % in the intensity of the white line, suggesting fewer accessible 3*p* holes due to Si-O hybridizations. A small unresolved shoulder (≈ 1843 eV, feature B in Fig. 8b) is observed for all spectra, which corresponds to distortions in the Si environment. This shoulder is attributed to transition of Si 1*s* electrons to the antibonding 3*s*-like state (Ildefonse *et al*., 1995; Li *et al.*, 1995). The resonance present at ≈ 1851 eV (feature C) is attributed to structural conformations equivalent to quartz according to the multiple scattering interpretation (Li *et al*., 1995), and resonances in the region of energies between 1856 eV and 1869 eV (between features D and E) can be described as a result of multiple scattering processes within the (SiO_4)-tetrahedron (Li *et al.*, 1995). As in the case of the white line, here some slight differences are observed for the KGa-2 sample and the spectra of the other three samples are equal to each other in this region. This can be explained because both the white line and this region are associated with the formation of SiO_4^{4-}-clusters that are affecting both hybridizations and the multiple scattering processes (Li *et al.;* 1994; Li *et al.*, 1995). Figure 8c presents the different Fourier transforms of the EXAFS oscillations for the studied samples, measured at the Si K-edge, together with the simulated spectrum from the structure determined from *ab initio* calculations (Richard & Rendtorff, 2019). The simulated spectrum possesses most of the characteristics found in the experimental measurements, which shows that the calculated structure is consistent with the X-ray absorption technique. As can be seen, the peaks of the simulated spectrum are always narrower than those obtained in the experimental samples; this could be explained by the presence of thermal vibrations in the lattice of the real samples, which are absent in the simulated one.

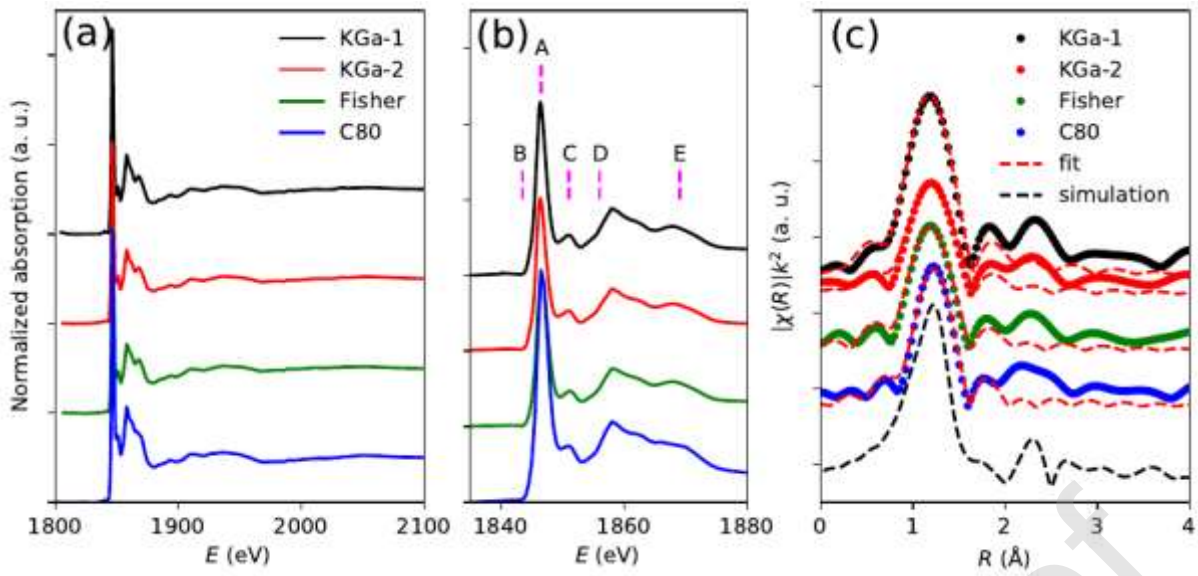

Figure 8. (a) Si K-edge absorption spectra, (b) XANES region of the absorption spectra, and (c) k^2-weighted Fourier transform of the extracted EXAFS oscillations. The dashed red lines in (c) stand for the fits, and the dashed black line corresponds to the simulated spectrum from the structure determined from *ab initio* calculations.

All experimental spectra have the same main contributions, which indicate that the atomic environment of Si atoms is very similar in all samples. A variation in the amplitude of the peak located at 1.2 Å (without phase correction) exists, which may be associated with the different degree of disorder present in the first coordination sphere of Si atoms. To check this hypothesis, nonlinear least-squares fits to the EXAFS signal for the clay samples were performed (dashed red lines in Fig. 8c). The fitting procedure was carried out with the coordination number fixed at 4, and the interatomic distance ($R_{Si\text{-}O}$) and the Debye-Waller factor ($DW_{Si\text{-}O}$) were obtained. Their values are included in Table 1.

For the case of C80 sample, where there is a significant amount of quartz, the fit was made by proposing two Si-O coordination spheres corresponding to the two main Si-containing phases present in the sample. The first one with fixed $R_{si\text{-}O}$ and DW factor corresponding to those reported for quartz (Li *et al.*, 1994), and using a coordination number fixed according to the presence of this phase in 55%. For the second one, a fixed coordination number according to the 45% proportion is used, and $R_{si\text{-}O}$ and the DW factor were left free in the fit. Table 1 shows both contributions parameters separately.

As can be seen, the basic structure of Si tetrahedral sites is practically the same in the four samples, but the local disorder described by the DW factor is different for each clay. According to the obtained values for DW factor, the local crystallinity increases following the order KGa-2, C80, Fisher, and KGa-1. It can be noted that DW factor values for KGa-1 and KGa-2 show a significant difference (3.6(1) x 10^{-3} Å^2 and 9.4(2) x 10^{-3} Å^2, respectively), which guarantees the sensitivity of the EXAFS technique for detecting the local disorder in this kind of material.

3.5. Discussion

In previous sections results from different experimental techniques were introduced and analyzed separately. First, the SEM images showed distinctive structural features for kaolinites at a micrometer scale, in agreement with micrographs for other clays reported in the literature (Frost *et al.*, 2002; Pietzsch et al., 2015; Andrini el al., 2016; Dill, 2016; Bukalo *et al.*, 2018). Then, a further extensive characterization was performed to the four kaolinites, spanning down to the Si local environments through the EXAFS technique. On the other hand, the comparison of the experimental XRD patterns and the EXAFS signals with the theoretical ones, obtained from an idealized defect-free kaolinites coming from first-principles calculations, gave additional references against which to compare the experimental data.

XRD, DTA/TGA, and EXAFS measurements allowed a wide structural characterization of the samples, which included the determination of the different order indices in each case. In this respect, the XRD-based indices, HI and R2, are quite direct methods to measure the sample order with very good accuracy when a high amount of kaolinite in the sample can be confirmed. In this sense, the applicability of such methods in the case of the C80 clay may be questionable due to the presence of quartz in the sample, and the consequent additional diffraction peaks in the XRD pattern in the region of interest.

The obtained results for the HI and R2 indices in KGa-1 and KGa-2 samples are in the range of those previously reported by other authors. As these kaolinites are well-established reference standards, it exist a good experimental background for their XRD-based indices. For HI, values ranges from 0.99 to 1.25 in KGa-1, and from 0.16 to 0.56 in KGa-2 (Uwins *et al.*, 1993; Bellotto, 1994; Aparicio & Galán, 1999; Vieira-Coelho *et al.*, 2000; Valášková *et al.*, 2011; Sakharov *et al.*, 2016). Also, for R2

index have been reported values in the range 0.97 to 1.01 in the case KGa-1, and in the range 0.63 to 0.76 in the case of KGa-2 (Aparicio & Galán, 1999; Vieira-Coelho *et al.*, 2000).

In this study, DTA/TGA measurements complemented the XRD results by considering the sample behavior under heating. In particular, the SR index showed a distinction between KGa-2 and C80 (both with the highest content of surface defects) and KGa-1 and Fisher samples (both with a SR value below 2). Furthermore, the analysis of T_{TGA} and T_{DTA} values, show the known correlation between kaolinite surface order and the dehydration reaction. Therefore, further analysis by examining a larger selection of samples, would be useful to better understand the relation between order/disorder and characteristic temperatures from this process, which may lead a new and better order index using these techniques.

On the other hand, this work presented for the first time a detailed study of EXAFS Si K-edge signals for different kaolinites, including measurements and theoretical predictions based on the structures calculated by first-principles methods. It was shown that EXAFS is a very sensitive technique for quantifying the structural order in kaolinite samples. In particular, the DW factor clearly distinguishes among the different samples. For example, in the case of KGa-1 and KGa-2, the DW values indicate that, from the point of view of the Si atoms, the local environments are more disordered in KGa-2 compared to KGa-1.

At this point, considering all the presented results, the general trend that summarizes a global comparison between samples is that KGa-1 and Fisher are the most ordered ones, C80 are more poorly ordered, and KGa-2 is the most disordered one. However, this classification must be taken with caution because, as stated above, each experimental technique helps to sense a different feature of the structural order, *i. e.*, while HI and R2 refer to the long-range order, SR serves to sense the surface order, and DW the local order. Even so, if the purpose is to find correlations between indices and samples, a closer look to the values reported in Table 1 can be done. In that sense, a detailed comparison between indices must take into account the sensitivity of each technique, and that the error bars for each index play a key role. In this respect, the relative errors are below 10% for HI, R2, and DW, and between 10 and 35% for SR. Furthermore, each index covers a different range of values to distinguish between order and disorder, so the relative weight of such error bars is different for each method.

Considering all these issues, and as an auxiliary parameter to compare the accuracy of the indices, it can be analyzed the relative deviation Δ for each index i from its value i_0 in a reference sample, $\Delta=|i-i_0|/i_0$ (i stands for HI, R2, SR or DW). This alternative approach assesses the capability of each index to distinguish between samples, using the structural ordering as the measuring instrument. In Fig. 9 the results for the Δ values are presented, where for each technique i_0 was chosen to be the value corresponding to the KGa-1 sample, because is the most ordered sample for all the considered indices (for the SR index both the Fisher and the KGa-1 samples are the most ordered if the error bar of this index is taken into account).

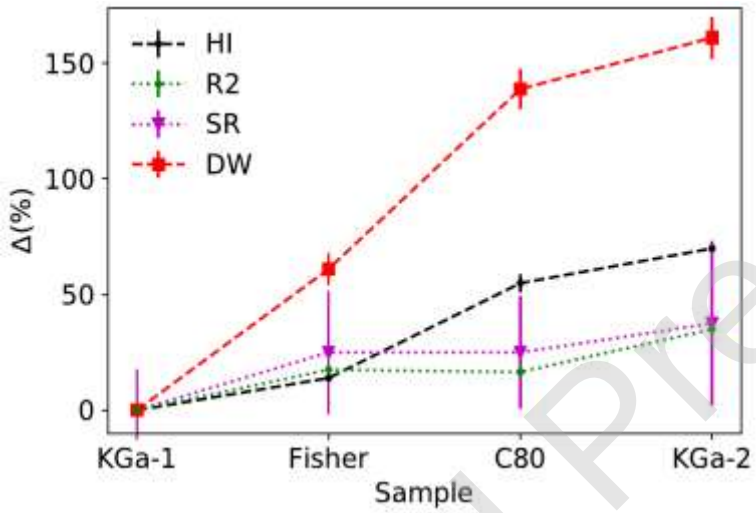

Figure 9. Relative deviation Δ (in percent) for the different indices, measured from the value corresponding to the KGa-1 sample (considered as the most ordered sample by all indices).

As can be seen in Fig. 9, the size of deviations Δ is different depending on the considered series. For example, R2 is characterized by a low relative error, but is not as sensitive as other indexes to a change from one kaolinite to another: it changes in about 40% from KGa-1 to KGa-2. A similar limitation can be found in the response of the SR index, with the inconvenience of having the highest relative error. On the contrary, the series corresponding to HI has a good balance between the size of Δ deviations and the index relative error, whereas DW presents the highest Δ deviations maintaining a low relative error. Based on the correlation between Δ values for HI and DW series, and the accessibility of X-ray diffractometer compared to a synchrotron beamline, this correlation could be used to infer kaolinite order globally *(i.e.*, from crystallographic to local) using the HI index.

Nevertheless, the performance of the DW index shown in this general comparison demonstrates that the Si K-edge EXAFS is still more effective for quantifying the structural order in kaolinite samples. The wide range of Δ obtained with DW indicates that, through this order index, EXAFS is able to discern the different kaolinite samples, which include intermediate cases between the standards KGa-1 and KGa-2 whose structural order can not be distinguished by other indices. So, EXAFS should be taken into account as a complementary one to XRD when the situation requires precision beyond XRD capabilities. This may occur with natural kaolinites and commercial clays that are typically involved in industrial processes.

4. Conclusions

Four kaolinite samples have been characterized by different experimental techniques. Their structural order at different scales (crystallographic/long-range, superficial, and local) was comprehensively analyzed. Among these samples, a local industrial kaolinitic clay was included to assess the reliability of each index on a sample of massive use. Additionally, XRD patterns and EXAFS signals corresponding to a theoretical defect-free kaolinite were considered as reference to compare with the experimental results, which gave a better understanding of the role of defects and additional phases in the samples.

It was shown that thermal analyses can provide insights to relate the structural order in kaolinites with characteristic temperatures observed in the DTA/TGA signals during the transition to metakaolinite. In general, the SR index from DTA has very large error bars, which make difficult to distinguish a highly ordered kaolinite from a disordered one. Further investigations on this respect may allow defining a new index based on the thermochemical analyses, better than SR, as well as a more comprehensive understanding of the kaolinite structure order-disorder upon heating.

The XRD-based R2 index has a similar performance as SR, being both the least sensitive and therefore, least recommended to use. On the contrary, the XRD-based HI index and the DW factor from EXAFS clearly distinguish between ordered and disordered samples. The first of them has the advantage of its easy access and simple measurement, although if the sample presents additional phases, such as quartz, it could lead to questionable results. In this sense, although the availability of

the EXAFS technique is more limited due to the experimental facilities it requires, this work showed that the DW parameter is the one with the best resolution, and is able to separate the contributions of possible additional Si phases. This point is very important when determining the degree of order on kaolins for industrial uses. So, in such cases complementary measurements to the well-established XRD are strongly recommended, and Si K-edge EXAFS emerges as a suitable technique in this respect.

Acknowledgements

This work has been supported by LNLS under Proposals SXS- 20180272 and SXS- 20190124, Consejo Nacional de Investigaciones Científicas y Técnicas (CONICET), Agencia Nacional de Promoción Científica y Tecnológica (ANPCyT, PICT 2016-1193), and Facultad de Ciencias Exactas, Universidad Nacional de La Plata (UNLP, X-904). JMM thanks CONICET for the scholarship. Authors also wish to thank Ricardo Anaya, Mariano Cipollone, and YPF Tecnología for the aid with the SEM images.

References

Andrini L., Gauna M. R., Conconi M. S., Suarez G., Requejo F. G., Aglietti E. F. & Rendtorff N. M. (2016) Extended and local structural description of a kaolinitic clay, its fired ceramics and intermediates: An XRD and XANES analysis. *Applied Clay Science*, **124–125**, 39–45. https://doi.org/10.1016/j.clay.2016.01.049

Andrini L., Moreira Toja R., Conconi M. S., Requejo F. G. & Rendtorff N. M. (2019) Halloysite nanotube and its firing products: Structural characterization of halloysite, metahalloysite, spinel type silicoaluminate and mullite. *Journal of Electron Spectroscopy and Related Phenomena*, **234**, 19–26. https://doi.org/10.1016/j.elspec.2019.05.007

Aparicio P. & Galán E. (1999) Mineralogical interference on kaolinite crystallinity. *Clays and Clay Minerals*, **47**, 12–27. https://doi.org/10.1346/CCMN.1999.0470102

Aparicio P., Galán E. & Ferrell R. E. (2006) A new kaolinite order index based on XRD profile fitting. *Clay Minerals*, **41**, 811–817. https://doi.org/10.1180/0009855064140220

Balan E., Fritsch E., Allard T. & Calas G. (2007) Inheritance vs. neoformation of kaolinite during lateritic soil formation: a case study in the middle Amazon Basin. Clays and Clay Minerals, **55**, 253–259. https://doi.org/10.1346/ccmn.2007.0550303

Barreto Maia A. A., Angélica R. S., de Freitas Neves R., Pöllmann H., Straub C. & Saalwächter K. (2014) Use of ^{29}Si and ^{27}Al MAS NMR to study thermal activation of kaolinites from Brazilian Amazon kaolin wastes. *Applied Clay Science*, **87**, 189–196. https://doi.org/10.1016/j.clay.2013.10.028

Bellotto M. (1994) High Temperature Phase Transitions in Kaolinite: The Influence of Disorder and Kinetics on the Reaction Path. *Materials Science Forum*, **166-169**, 3–22. https://doi.org/10.4028/www.scientific.net/msf.166-169.3

Beni G. & Platzman P. M. (1976) Temperature and polarization dependence of extended x-ray absorption fine-structure spectra. *Physics Review B*, **14**, 1514–1518. https://doi.org/10.1103/PhysRevB.14.1514

Bich Ch., Ambroise J. & Péra J. (2009) Influence of degree of dehydroxylation on the pozzolanic activity of metakaolin. *Applied Clay Science*, **44**, 194–200. https://doi.org/10.1016/j.clay.2009.01.014

Bish L. (1993) Rietveld refinement of the kaoilinite structure at 1.5 K. *Clays and Clay Minerals*, **41**, 738–744. https://doi.org/10.1346/CCMN.1993.0410613

Brigatti M. F., Galan E. & Theng B. K. G. (2006) Structures and mineralogy of clay minerals. *Developments in Clay Science*, **1**, 19–86. https://doi.org/10.1016/S1572-4352(05)01002-0

Brindley G. W. & Robinson K. (1945) Structure of kaolinite. *Nature*, **156**, 661–662. https://doi.org/10.1038/156661b0

Bukalo N. N., Ekosse G. I. E., Odiyo J. O. & Ogola J. S. (2018) Mineralogical characteristics of Cretaceous-Tertiary kaolins of the Douala Sub-Basin, Cameroon. *Journal of African Earth Sciences*, **141**, 130–147. https://doi.org/10.1016/j.jafrearsci.2018.02.010

Bunker G. (2010) *Introduction to XAFS. A Practical Guide to X-ray Absorption Fine Structure Spectroscopy*. Cambridge University Press, UK, 260 pp.

Chaboy J., Barranco A., Yanguas-Gil A., Yubero F. & González-Elipe A. R. (2007) Si K-edge XANES study of $SiO_xC_yH_z$ amorphous polymeric materials. *Physics Review B*, **75**, 075205. https://doi.org/10.1103/PhysRevB.75.075205

Chakraborty K. (2014) *Phase transformation of kaolinite clay*. Springer, New Delhi, India, 342 pp. https://doi.org/10.1007/978-81-322-1154-9

Chipera S. J. & Bish D. L. (2001) Baseline Studies of the Clay Minerals Society Source Clays: Powder X-ray Diffraction Analyses. *Clays and Clay Minerals*, **49**, 398–409. https://doi.org/10.1346/CCMN.2001.0490507

Conconi M. S., Gauna M. R., Serra M. F., Suarez G., Aglietti E. F. & Rendtorff N. M. (2014) Quantitative firing transformations of a triaxial ceramic by X-ray diffraction methods. *Cerâmica*, **60**, 524–531. https://doi.org/10.1590/S0366-69132014000400010

Conconi M. S., Morosi M., Maggi J., Zalba P. E., Cravero F. & Rendtorff N. M. (2019) Thermal behavior (TG-DTA-TMA), sintering and properties of a kaolinitic clay from Buenos Aires Province, Argentina. *Cerâmica*, **65**, 227–235. https://doi.org/10.1590/0366-69132019653742621

Danner T., Norden G. & Justnes H. (2018) Characterisation of calcined raw clays suitable as supplementary cementitious materials. *Applied Clay Science*, **162**, 391–402. https://doi.org/10.1016/j.clay.2018.06.030

Dill H. G. (2016) Kaolin: Soil, rock and ore; from the mineral to the magmatic, sedimentary and metamorphic environments. *Earth-Science Reviews*, **161**, 16–129. https://doi.org/10.1016/j.earscirev.2016.07.003

Drits V. A., Sakharov B. A., Dorzhieva O. V., Zviagina B. B. & Lindgreen H. (2019) Determination of the phase composition of partially dehydroxylated kaolinites by modelling their X-ray diffraction patterns. *Clay Minerals*, **54**, 309–322. https://doi.org/10.1180/clm.2019.39

Dumas A., Mizrahi M., Martin F. & Requejo F. G. (2015) Local and extended-order evolution of synthetic talc during hydrothermal synthesis: Extended X-ray Absorption Fine Structure, X-ray Diffraction, and Fourier Transform Infrared Spectroscopy studies. *Crystal Growth & Design*, **15**, 5451–5463. https://doi.org/10.1021/acs.cgd.5b01076

Frost R. L., van Der Gaast S. J., Zbik M., Kloprogge J. T. & Paroz G. N. (2002) Birdwood kaolinite: a highly ordered kaolinite that is difficult to intercalate. An XRD, SEM and Raman spectroscopic study. *Applied Clay Science*, **20**, 177–187. https://doi.org/10.1016/S0169-1317(01)00071-0

Gadikota G., Zhang F. & Allen A. (2017) In situ angstrom-to-micrometer characterization of the structural and microstructural changes in kaolinite on heating using Ultrasmall-Angle, Small-Angle, and Wide-Angle X- ray Scattering (USAXS/SAXS/WAXS). *Industrial & Engineering Chemistry Research*, **56**, 11791–11801. https://doi.org/10.1021/acs.iecr.7b02810

Guggenheim S., Bain D. C., Bergaya F., Brigatti M. F., Drits V. A., Eberl D. E., Formoso M. L. L., Galán E., Merriman R. J., Peacor D. R., Stanjek H. & Watanabe T. (2002) Report of the association internationale pour l'étude des argiles (AIPEA) nomenclature committee for 2001: Order, disorder and crystallinity in phyllosilicates and the use of the "crystallinity index". *Clays and Clay Minerals*, **50**, 406–409. https://doi.org/10.1346/000986002760833783

Heide K. & Földvari M. (2006) High temperature mass spectrometric gas-release studies of kaolinite $Al_2[Si_2O_5(OH)_4]$ decomposition. *Thermochimica Acta*, **446**, 106–112. https://doi.org/10.1016/j.tca.2006.05.011

Hinckley D. (1963) Variability in 'crystallinity' values among the kaolin deposits of the Coastal Plain of Georgia and South Carolina. Pp. 229–235 in: *Proceedings of the 11th International Conference on Clays and Clay Minerals* (W. F. Bradley, editor).

Ildefonse Ph, Calas G., Flank A. M. & Lagarde P. (1995) Low Z elements (Mg, Al, and Si) K-edge X-ray absorption spectroscopy in minerals and disordered systems. *Nuclear Instruments and Methods in Physics Research B*, **97**, 172–175. https://doi.org/10.1016/0168-583x(94)00710-1

Johnston T. (2010) Probing the nanoscale architecture of clay minerals. *Clay Minerals*, **45**, 245–279. https://doi.org/10.1180/claymin.2010.045.3.245

Kloprogge J. (2019) *Spectroscopic methods in the study of kaolin minerals and their modifications.* Springer Mineralogy, Switzerland, 428 pp. https://doi.org/10.1007/978-3-030-02373-7

Kroll P. & Milko M. (2003) Theoretical Investigation of the Solid State Reaction of Silicon Nitride and Silicon Dioxide forming Silicon Oxynitride (Si_2N_2O) under Pressure. *Zeitschrift für anorganische und allgemeine Chemie*, **629**, 1737–1750. https://doi.org/10.1002/zaac.200300122

La Iglesia A. (1993) Pressure induced disorder in kaolinite. *Clay Minerals*, **28**, 311–319. https://doi.org/10.1180/claymin.1993.028.2.11

Lee P. A., Citrin P. H., Eisenberger P. & Kincaid B. M. (1981) Extended x-ray absorption fine structure-its strengths and limitations as a structural tool. *Reviews of Mododern Physics*, **53**, 769–806. https://doi.org/10.1103/RevModPhys.53.769

Leonardi A. & Bish D. L. (2020) Understanding powder X-ray diffraction profiles from layered minerals: the case of kaolinite nanocrystals. *Inorganic Chemistry*, **59**, 5357–5367. https://doi.org/10.1021/acs.inorgchem.9b03464

Li D., Bancroft G. M., Kasrai M., Fleet M. E., Secco R. A., Feng X. H., Tan K. H. & Yang B. X. (1994) X-ray absorption spectroscopy of silicon dioxide (SiO_2) polymorphs: The structural characterization of opal. *American Mineralogist*, **79**, 622–632.

Li D., Bancroft G. M., Fleet M. E., & Feng X. H. (1995) Silicon K-edge XANES spectra of silicate minerals. *Physics and Chemistry of Minerals*, **22**(2), 115-122. https://doi.org/10.1007/BF00202471

Li J., Zuo X., Zhao X., Ouyang J. & Yang H. (2019) Insight into the effect of crystallographic structure on thermal conductivity of kaolinite nanoclay. *Applied Clay Science*, **173**, 12–18. https://doi.org/10.1016/j.clay.2019.03.011

Lietard O. (1977) *Contribution à l' étude des propiétés phisicochimiques, cristallographiques et morphologiques des kaolins*. Thèse Doc. Sci. Phys., Nancy, France, 345 pp.

Mermut A. R. & Cano A. F. (2001) Baseline studies of The Clay Mineral Society Source Clays: Chemical analyses of major elements. *Clays and Clay Minerals*, **49**, 381–386. https://doi.org/10.1346/CCMN.2001.0490504

Momma K. & Izumi F. (2011) VESTA 3 for three-dimensional visualization of crystal, volumetric and morphology data. *Journal of Applied Crystallography*, **44**, 1272–1276. https://doi.org/10.1107/S0021889811038970

Moreno Erazo A. X. (2014) *Obtención tecnológica de mullita a partir de arcillas y caolines refractarios argentinos, y alúmina calcinada o alúminas hidratadas.* PhD Thesis. Universidad Nacional de La Plata, La Plata, Argentina, 301 pp. https://doi.org/10.35537/10915/36815

Neder R. B., Burghammer M., Grasl T. H., Schulz H., Bram M., Fiedler S. (1999) Refinement of the kaolinite structure from single crystal synchrotron data. *Clays and Clay Minerals*, **47**, 487–494. https://doi.org/10.1346/CCMN.1999.0470411.

Newville, M. (2001). IFEFFIT: interactive XAFS analysis and FEFF fitting. Journal of synchrotron radiation, 8(2), 322-324. https://doi.org/10.1107/S0909049500016964

Organova N. I., Nasdekin V. V., Rozhdestvenskaya I. V., Marsii I. M., Ivanova T. I., Zakharov N. D. & Borisovskii S. B. (1999) Structures of the K- and Na-components of two-phase feldspar from Primore. *Kristallografiya*, **44**, 829–834.

Paris M. (2014) The two aluminum sites in the ^{27}Al MAS NMR spectrum of kaolinite: Accurate determination of isotropic chemical shifts and quadrupolar interaction parameters. *American Mineralogist*, **99**, 393–400. https://doi.org/10.2138/am.2014.4607

Pietzsch A., Nisar J., Jämstorp E., Gråsjö J., Århammar C., Ahuja R. & Rubensson J.-E. (2015) Kaolinite: Defect defined material properties – A soft X-ray and first principles study of the band gap. *Journal of Electron Spectroscopy and Related Phenomena*, **202**, 11–15. http://dx.doi.org/10.1016/j.elspec.2015.02.003

Plançon A., Giese R. F. & Snyder R. (1988) The Hinckley index for kaolinites. *Clay Minerals*, **23**, 249–260. https://doi.org/10.1180/claymin.1988.023.3.02

Rashad M. (2013) Metakaolin as cementitious material: History, scours, production and composition - A comprehensive overview. *Construction and Building Materials*, **41**, 303–218. https://doi.org/10.1016/j.conbuildmat.2012.12.001

Ravel B. & Newville M.(2005) ATHENA, ARTEMIS, HEPHAESTUS: data analysis for X-ray absorption spectroscopy using IFEFFIT. *Journal of Synchrotron Radiation*, **12**, 537–541. https://doi.org/10.1107/S0909049505012719

Rehr J. J., Kas J. J., Vla F. D., Prange M. P. & Jorissen K. (2010) Parameter-free calculations of X-ray spectra with FEFF9. *Physical Chemistry Chemichal Physics*, **12**, 5503–5513. https://doi.org/10.1039/B926434E

Richard D. & Rendtorff N. M. (2019) First principles study of structural properties and electric field gradients in kaolinite. *Applied Clay Science*, **169**, 67–73. https://doi.org/10.1016/j.clay.2018.12.013

Rivard C., Montargès-Pelletier E., Vantelon D., Pelletier M., Karunakaran C., Michot L. J., Villieras F. & Michau N. (2013) Combination of multi-scale and multi-edge X-ray spectroscopy for investigating the products obtained from the interaction between kaolinite and metallic iron in anoxic conditions at 90 °C. *Physics and Chemistry of Minerals*, **40**, 115–132. https://doi.org/10.1007/s00269-012-0552-6

Sakharov B. A., Drits V. A., McCarty D. K. & Walker G. M. (2016) Modeling powder X-ray diffraction patterns of the Clay Minerals Society kaolinite standards: KGa-1, KGa-1b, and Kga-2. *Clays and Clay Minerals*, **64**, 314–333. https://doi.org/10.1346/CCMN.2016.0640307

Schroeder P. A. & Erickson G. (2014) Kaolin: From ancient porcelains to nanocomposites. *Elements*, **10**, 177–182. https://doi.org/10.2113/gselements.10.3.177

Sei J., Morato F., Kra G., Staunton S., Quiquampoix H., Jumas J. C. & Olivier-Fourcade J. (2006) Mineralogical, crystallographic and morphological characteristics of natural kaolins from the Ivory Coast (West Africa). *Journal of African Earth Sciences*, **46**, 245–252. https://doi.org/10.1016/j.jafrearsci.2006.06.002

Serra M. F., Conconi M. S., Suarez G., Agietti E. F. & Rendtorff N. M. (2013) Firing transformations of an Argentinean calcareous commercial clay. *Cerâmica*, **59**, 254–261. https://doi.org/10.1590/S0366-69132013000200010

Sevillano E., Meuth H. & Rehr J. J. (1979) Extended x-ray absorption fine structure Debye-Waller factors. I. Monatomic crystals. *Physical Review B*, **20**, 4908–4911. https://doi.org/10.1103/PhysRevB.20.4908

Steudel A., Mehl D. & Emmerich K. (2013) Simultaneous thermal analysis of different bentonite–sodium carbonate systems: an attempt to distinguish alkali-activated bentonites from raw materials. *Clay Minerals*, **48**, 117–128. https://doi.org/10.1180/claymin.2013.048.4.08

Tironi A., Trezza M. A., Scian A. N. & Irassar E. F. (2012) Kaolinitic calcined clays: factors affecting its performance as pozzolans. *Construction and Building Materials*, **28**, 276–281. https://doi.org/10.1016/j.conbuildmat.2011.08.064

Tironi A., Trezza M. A., Scian A. N. & Irassar E. F. (2014) Thermal analysis to assess pozzolanic activity of calcined kaolinitic clays. *Journal of Thermal Analysis and Calorimetry*, **117**, 547–556. https://doi.org/10.1007/s10973-014-3816-1

Tunega D., Bučko T. & Zaoui A. (2012) Assessment of ten DFT methods in predicting structures of sheet silicates: Importance of dispersion corrections. *The Journal of Chemical Physics*, **137**, 114105. https://doi.org/10.1063/1.4752196

Uwins P. J. R., Mackinnon I. D. R., Thomson J. G. & Yago A. J. E. (1993) Kaolinite: NMF intercalates. *Clays and Clay Minerals*, **41**, 707–717. https://doi.org/10.1346/CCMN.1993.0410609

Valášková M., Barabaszová K., Hundáková M., Ritz M. & Plevová E. (2011) Effects of brief milling and acid treatment on two ordered and disordered kaolinite structures. *Applied Clay Science*, **54**, 70–76. https://doi.org/10.1016/j.clay.2011.07.014

Vieira-Coelho A. C., Montes C. R., Valera T. S. (2000) Estudo do grau de ordem/desordem estrutural de caulinitas em caulins da Região Amazônica por Difratometria de raios-X. Pp 201–213 in: *Anais do 44º Congresso Brasileiro de Cerâmica* (Associação Brasileira de Cerâmica, editor).

Weck P. F., Kim E. & Jové-Colón C. F. (2015) Relationship between crystal structure and thermo-mechanical properties of kaolinite clay: beyond standard density functional theory. *Dalton Transactions*, **44**, 12550–12560. https://doi.org/10.1039/c5dt00590f

Weirich Th. E., Winterer M., Seifried S., Hahn H., Fuess H. (2000) Rietveld analysis of electron powder diffraction data from nanocrysalline anatase, TiO_2. *Ultramicroscopy*, **81**, 263–270. https://doi.org/10.1016/S0304-3991(99)00189-8

White E., Provis J. L., Proffen T., Riley D. P. & van Deventer J. S. J. (2010) Density Functional modeling of the local structure of kaolinite subjected to thermal dehydroxylation. *The Journal of Physical Chemistry A*, **114**, 4988–4996. https://doi.org/10.1021/jp911108d

White C. E., Perander L. M., Provis J. L., & Van Deventer,J. S. (2011) The use of XANES to clarify issues related to bonding environments in metakaolin: a discussion of the paper S. Sperinck et al.,

"Dehydroxylation of kaolinite to metakaolin-a molecular dynamics study," J. Mater. Chem., 2011, 21, 2118–2125. *Journal of Materials Chemistry*, **21**(19), 7007-7010.
https://doi.org/10.1039/C1JM10379B

White E., Kearley G. J., Provis J. L. & Riley D. P. (2013) Inelastic neutron scattering analysis of the thermal decomposition of kaolinite to metakaolin. *Chemical Physics*, **427**, 82–86.
https://doi.org/10.1016/j.chemphys.2013.08.009

Tables and Illustrations with captions

	XRD		**DTA/TGA**			**EXAFS**	
Sample	**HI**	**R2**	T_{TGA} **(°C)**	T_{DTA} **(°C)**	**SR**	$R_{Si\text{-}O}$ **(Å)**	$DW_{Si\text{-}O}$ **(x10^{-3} Å^2)**
KGa-1	0.999(9)	0.97(1)	571	580	1.6(2)	1.62(1)	3.6(1)
KGa-2	0.30(2)	0.63(2)	556	571	2.2(5)	1.61(1)	9.4(2)
Fisher	0.86(2)	0.80(2)	598	612	1.2(4)	1.62(1)	5.8(2)
C80	0.45(4)	0.81(2)	547	565	2.0(3)	1.61* 1.62(1)	2.0* 8.6(2)

Table 1. Results for the different samples by XRD, DTA/TGA, and EXAFS: Hinckley Index (HI), R2 index after Lietard, kaolinite-metakaolinite transition temperatures from TGA (T_{TGA}) and DTA (T_{DTA}), Slope Ratio index (SR), Si-O interatomic distance ($R_{Si\text{-}O}$) and the Debye-Waller factor ($DW_{Si\text{-}O}$). For

each value, the number in parentheses is the error in the last digit. *These parameters were kept fixed in the fit and correspond to the quartz phase.

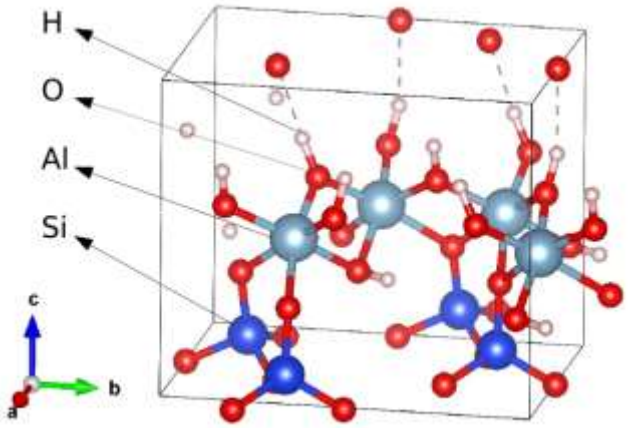

Figure 1. Structure of kaolinite and unit cell.

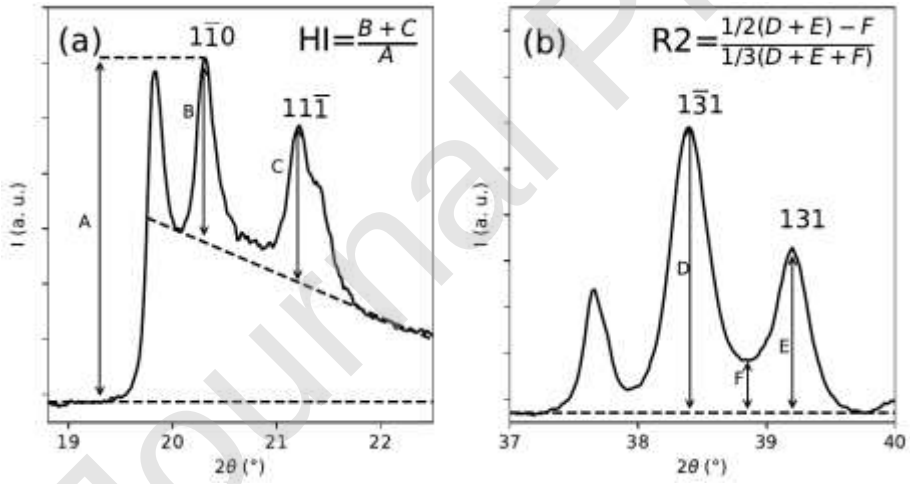

Figure 2. Method for the determination of order indices based on XRD: (a) HI and (b) R2.

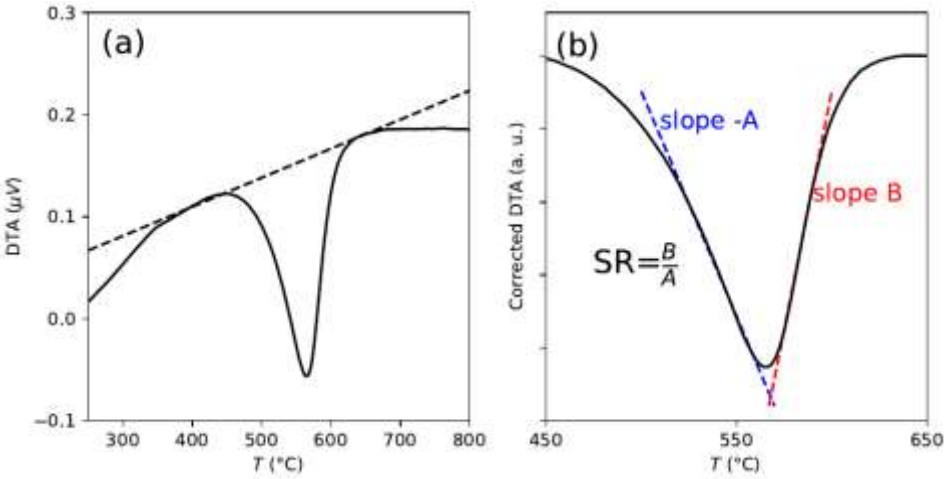

Figure 3. Method for the determination of the SR index based on DTA endothermic peak. (a) DTA curve and local background to be subtracted, and (b) corrected curve after background subtraction. The quantities A and B are defined positive.

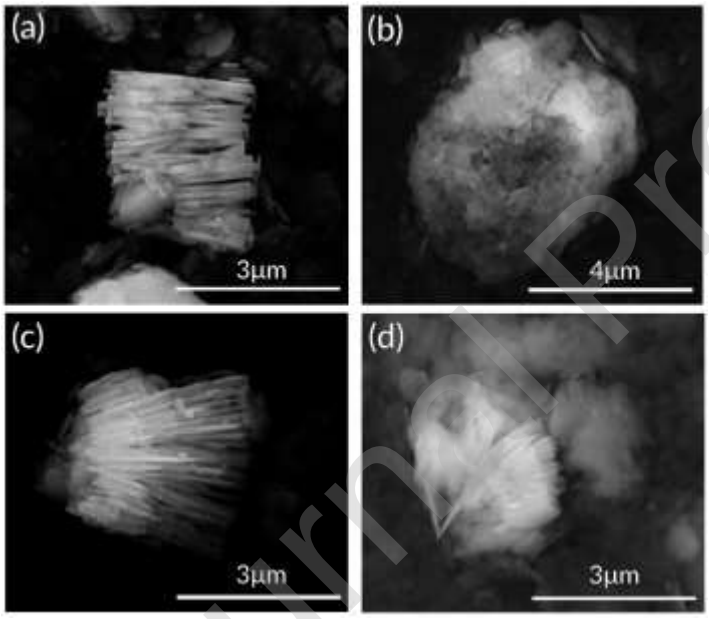

Figure 4. SEM images of the studied clays (a) KGa-1, (b) KGa-2, (c) Fisher, and (d) C80.

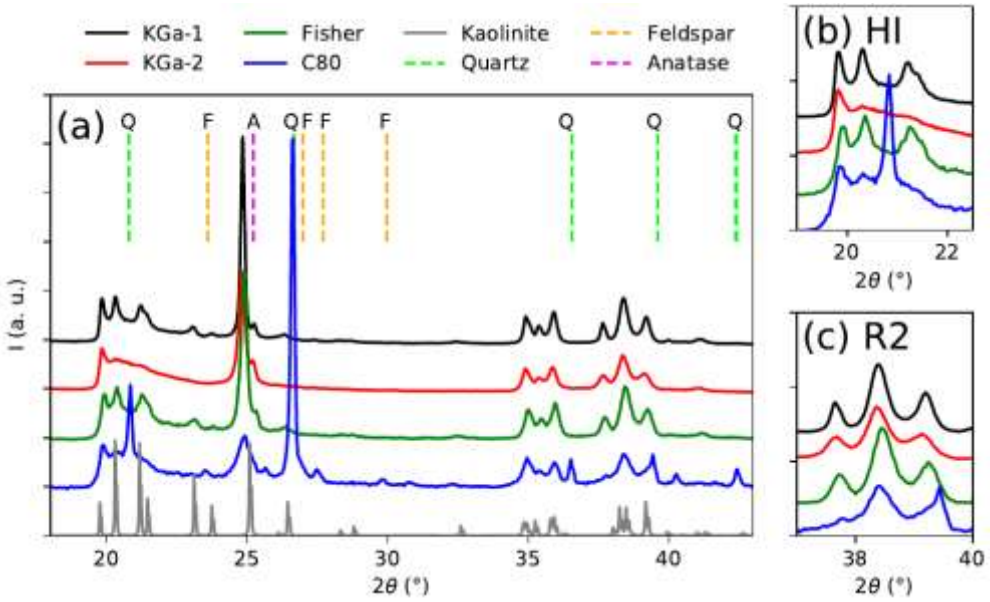

Figure 5. XRD patterns for the different samples. (a) Complete XRD patterns. The gray pattern in the bottom stands for the simulated pattern from the first-principles calculated structure of kaolinite (Richard & Rendtorff, 2019), while peaks of usual additional phases are indicated in the top. (b) Detail of the region corresponding to HI peaks and (c) R2 peaks.

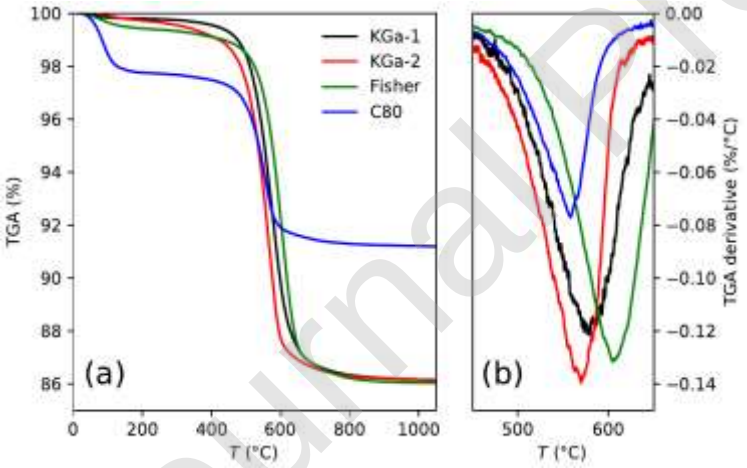

Figure 6. (a) TGA curves and (b) TGA derivatives (weight loss rate) in the kaolinite-metakaolinite transition region.

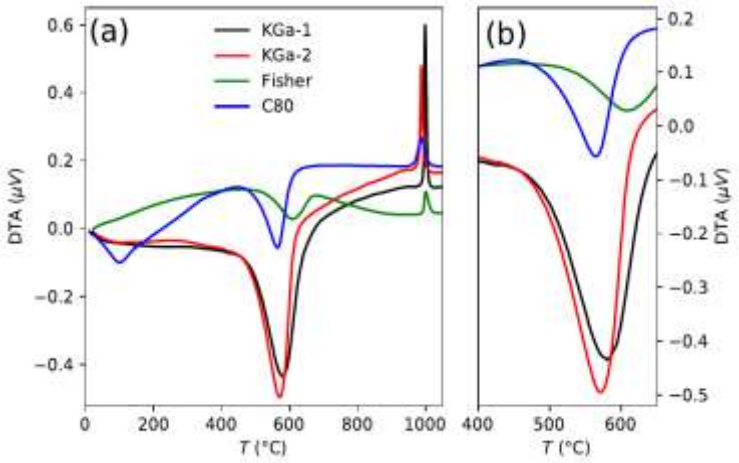

Figure 7. (a) DTA curves and (b) detail of the endothermic peaks corresponding to the kaolinite-metakaolinite transition.

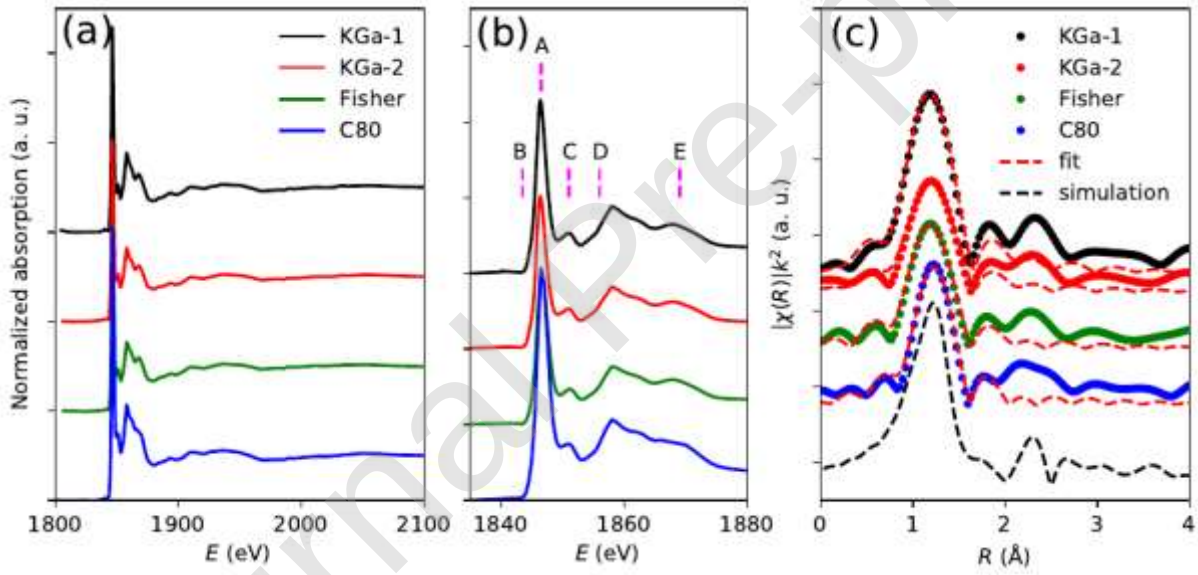

Figure 8. (a) Si K-edge absorption spectra, (b) XANES region of the absorption spectra, and (c) k^2-weighted Fourier transform of the extracted EXAFS oscillations. The dashed red lines in (c) stand for the fits, and the dashed black line corresponds to the simulated spectrum from the structure determined from *ab initio* calculations.

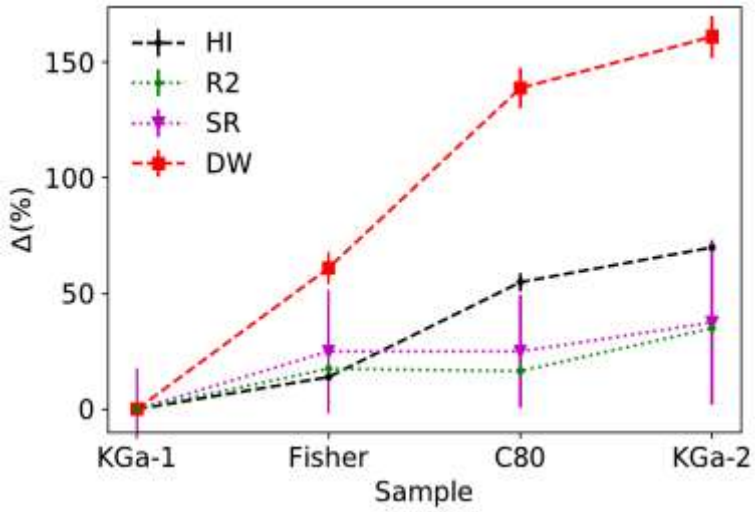

Figure 9. Relative deviation Δ (in percent) for the different indices, measured from the value corresponding to the KGa-1 sample (considered as the most ordered sample by all indices).